Monolithically integrated two-dimensional arrays of surface-emitting photonic-crystal terahertz lasers

G. Sevin, G. Xu, N. Isac, R. Colombelli, H. E. Beere & D. A. Ritchie

Volume 34 • Numbers 3–4 • April 2

Journal of Infrared, Millimeter, and Terahertz Waves

ONLINE FIRST

Springer

Springer

Monolithically integrated two-dimensional arrays of surface-emitting photonic-crystal terahertz lasers

G. Sevin · G. Xu · N. Isac · R. Colombelli · H. E. Beere · D. A. Ritchie

Abstract We demonstrate two-dimensional arrays of surface-emitting THz frequency photonic-crystal quantum cascade lasers covering a broad spectral range. The arrays are made of 16 unit elements, each of them spectrally single mode and featuring a narrow divergence emission pattern. The array emission frequencies cover a range of ≈0.2 THz around an emission frequency of ≈2.75 THz. Large size and small size devices have been developed. The former devices operate up to a maximum temperature of ≈90K with 2 to 3 mW output power in continuous wave regime.

Terahertz (THz) quantum cascade lasers (QCL) have become a promising semiconductor laser source for the 1.2 – 5 THz frequency range (λ = 250 – 60 μm) [1–3]. Applications include astronomy, (bio)-imaging and spectroscopy. Current research in the field is focused not only on increasing the maximum operating temperature (T_{max}, which is still limited to below-Peltier cooling temperatures), but also on a wide range of topics, such as 'beam-shaping' [4–7], ultra-fast modulation [8], sub-wavelength devices [9–11], inter alia.

Well-behaved surface emission can be achieved using photonic-crystal QCLs [4, 12–14], which furthermore offer single frequency output. However, frequency tunability of THz QCLs, and of QC lasers in general, is an open problem, whose solution would enable applications in spectroscopy and multi-spectral imaging [15, 16]. A possible alternative is represented by *on-chip tunability*, where arrays of single-mode devices emitting at closely spaced frequencies are implemented on a single chip [17, 18].

In this respect, surface-emitting devices are particularly attractive. While in fact edge emitting devices permit only one-dimensional arrangements, integration of two-dimensional arrays becomes possible with surface emission [17]. Recently, we have demonstrated that metallic photonic

G. Sevin · G. Xu · N. Isac · R. Colombelli (✉)
Institut d'Electronique Fondamentale, Univ. Paris Sud, UMR8622 CNRS, 91405 Orsay, France
e-mail: raffaele.colombelli@u-psud.fr

H. E. Beere · D. A. Ritchie
Cavendish Laboratory, University of Cambridge, Cambridge CB3 OHE, UK

🖄 Springer

crystals combined with THz QCLs lead to reproducible engineering of the spectral and spatial beam properties of the devices. In this letter, we present surface emitting 2D broadband PhC THz QCL arrays.

The THz QCL active region used (V414, same wafer as in Ref. [19]) is based on a bound-to-continuum design with nominal operation frequency at 2.7 THz, whose details can be found in Ref. [20]. The sample was grown by molecular beam epitaxy. The active region – 12 μm thick (90 active region and injector stages) - is sandwiched between 700 nm, 2E18 cm³, and 80 nm, 5E18 cm³ doped layers forming the lower and upper contacts. Two quantum wells in the injector superlattice were n-doped at levels of 1.6E16 cm³. A 300 nm-thick $Al_{0.50}Ga_{0.50}As$ etch stop layer was grown between the substrate and the lower contact layer.

The device fabrication started with Au-Au thermo-compressive wafer-bonding onto a GaAs carrier wafer, followed by host substrate removal with citric acid. Subsequently the n⁺-GaAs top contact was thinned from 700 to 200 nm to reduce the losses [3]. We then implemented 16-elements (4 × 4) arrays of PhC THz lasers based on the *optimized* design reported in Ref. [12]. In this paper we report results for arrays of 10-by-10 and 18-by-18 period devices, as reported in Fig. 1. This optimized design permits wire bonding in the device centre, as it was shown explicitly that the electromagnetic near-field in the central part of the device is not associated with the surface emission process, thus rendering this region redundant.

The grading of the holes size is carefully optimized to enhance the in-plane quality factor, and the introduction of a π phase-shift in the centre of the PhC structure leads to single lobed surface emission [5]. The emission frequency in a PhC scales with the lattice spacing, hence lithographic frequency tunability is achieved by implementing 16 devices with different periods, in steps of 0.2 μm. After substrate thinning and back-contact deposition, the samples were cleaved and mounted in a cryostat for the measurements.

Figure 2 shows the typical emission spectra – at intermediate currents - of the two laser arrays at cryogenic temperatures. The devices operate in single mode and the array elements
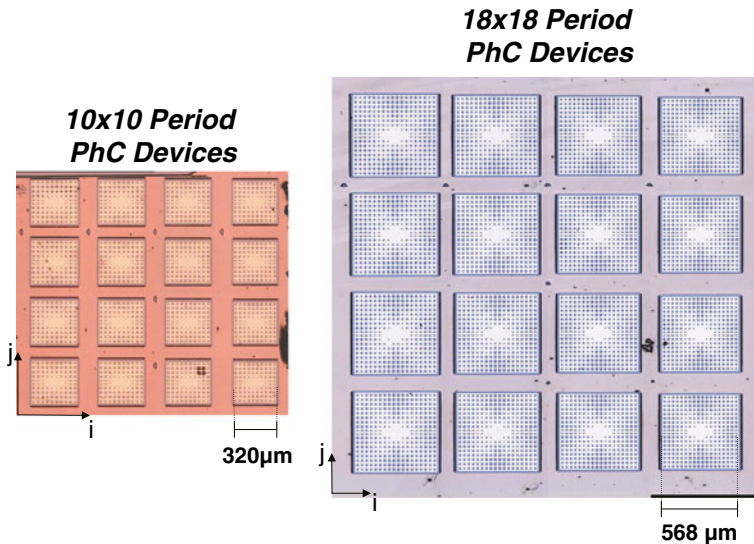
Fig. 1 Optical microscope image of monolithically integrated, 4 × 4 arrays of PhC QCL devices. Left panel: 10-by-10 period devices. The period ranges from 32.0 μm to 35.0 μm, in steps of 0.2 μm along the j axis and 0.8 μm along the i axis. Right panel: 18-by-18 period devices. The period ranges from 31.0 μm to 34.0 μm with the same step

Array of 10x10 PhC devices **Array of 18x18 PhC devices**
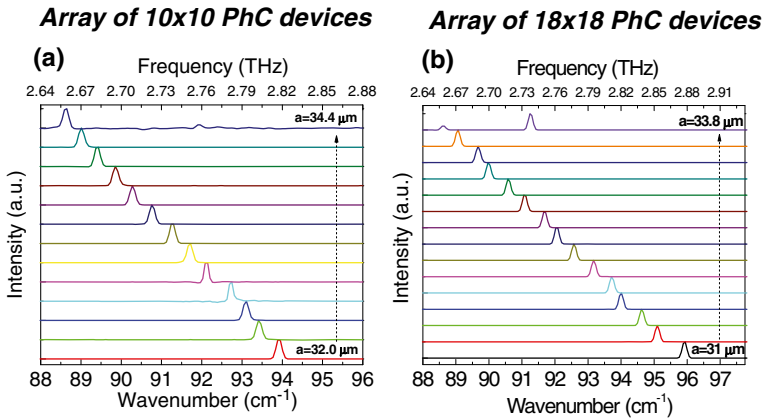
Fig. 2 Emission spectra of the arrays of PhC devices at low operating currents. (A) Data for the 10-by-10 period lasers. The PhC period ranges from 32.0 μm to 34.4 μm. (B). Data for the 18-by-18 period devices. The PhC period ranges from 31.0 μm to 33.8 μm. In both cases the emission correctly lithographically-tune with the PhC lattice spacing, covering a frequency span of 170 and 210 GHz, respectively. The spectra of the devices with larger periods are not included because the monopolar mode frequency lie outside the gain spectra. The spectra are measured with a FTIR spectrometer, in rapid scan mode, using a DTGS detector. The typical operating conditions are 300/500 ns pulse width and 30 kHz repetition rate

emission frequency correctly scales with the PhC period. Note: the two devices with the longest PhC periods are not completely single mode, possibly because the PhC is in this case tuned far from the peak gain. The lack of mode hopping proves that the devices correctly operate on the monopolar mode. This is an additional advantage of PhC-based devices. The array is a *sampled* version of a widely tunable laser source. The frequency step is ≈15 GHz, and the frequency span is 170 GHz and 210 GHz, respectively, for the small and large array. The central operating frequency of the array is ≈2.75 THz, which corresponds to the peak gain of the active laser material employed. Side mode suppression ratios between 20 and 30 dB are typically obtained (data not shown).

Figures 3A and 3B report the light-voltage-current density (LVJ) characteristics of selected array elements. The 10-by-10 period PhC THz lasers (Fig. 3A) exhibit typical threshold current densities (J_{th}) of 120/130 Acm^{-2}, and well reproducible, superposing J-V characteristics. The peak output power is 350/400 μW, with an upper limit of almost 0.5 mW and a lower limit of ≈150 μW.

The 18-by-18 period PhC THz lasers (Fig. 3B) exhibit lower J_{th} of ≈ 100 Acm^{-2}, and typical peak output powers of 3 mW, with an upper limit of 3.5 mW and a lower limit of ≈ 0.9 mW. All the devices, given the low applied bias and the low J_{th}, also operate in continuous-wave regime, with average output powers similar to the peak output power measured in pulsed regime. The estimated wall-plug efficiency (WPE) is ≈0.03% for the 10-by-10 period devices, and ≈0.08% for the 18-by-18 period devices. These low values for the WPE, compared with the current state-of-art of ≈ 0.3/0.5% for single-plasmon edge emitting devices, stems from the fact that these devices operate on non-radiative monopolar states of the PhC lattice [12]. All the measurements have been performed in open atmosphere, not under nitrogen purge. We believe therefore that the variability in the measured output power is due to atmospheric water absorption. This effect is even more pronounced since the devices emit spectrally single mode. Measuring the output power under nitrogen purge could also lead to higher WPEs. Note however that the wall-plug efficiency can be significantly improved by operating the devices on *radiative modes* instead [21]. In the final part of the

(a) *10x10 PhC devices*

(b) *18x18 PhC devices*
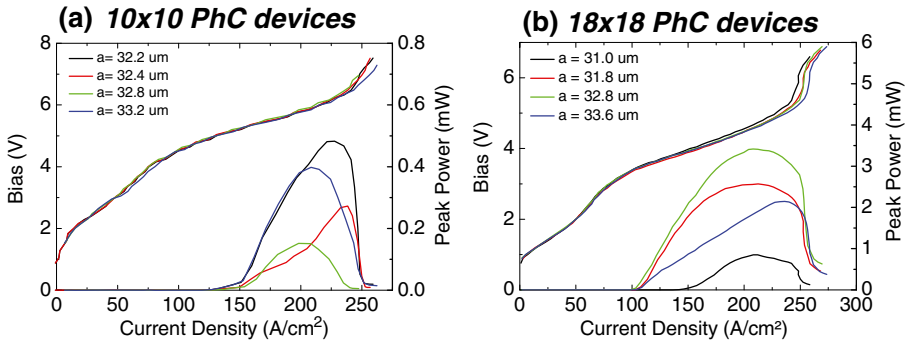
Fig. 3 (A) Light-voltage–current density (L-V-J) characteristics for four 10-by-10 period devices, at a temperature of 7K. (B) L-V-J characteristics for four 18-by-18 period devices at a temperature of 7K. Peak output powers of more than 3 mW are obtained, in a non-purged atmosphere. The measurements are performed at 4% duty cycle, but the devices can operate up to CW given the low threshold current density. The power calibration has been performed with a Thomas Keating Absolute THz power meter, which allowed us also to calibrate the internal DTGS of the spectrometer

paper we will show that such devices can be implemented – thanks to the recently developed concept of *graded photonic heterostructures* – and we'll make a comparison between the two technologies.

Figure 4 shows the typical temperature dependence of the J_{th} for an 18-by-18 period PhC THz laser, from 20K up to 85K. This latter temperature is the typical T_{max} for these devices. Note that the same material operates up to 95K if processed in standard metal-metal ridge configuration. The implementation of the PhC architecture therefore imposes only a very small price in the maximum operating temperature, in exchange of single-mode emission, and well behaved far-field emission patterns.

Typical experimental far-field patterns are reported in Fig. 5. They were acquired by scanning a Golay cell on a sphere at constant radius (approximately 12 cm) from the laser surface. The central, small inset defines the scanning angles. The 18-by-18 period devices exhibit an almost ideal, single-lobed angularly-narrow emission pattern. The single-lobed
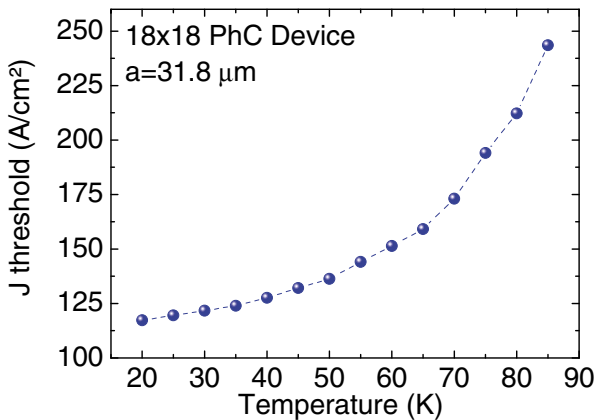
Fig. 4 Threshold current density (J) as a function of temperature for an 18-by-18 period laser with 31.8 μm PhC period. All the measurements have been performed at 2% duty-cycle (500 ns long pulses, at a frequency of 40 kHz)
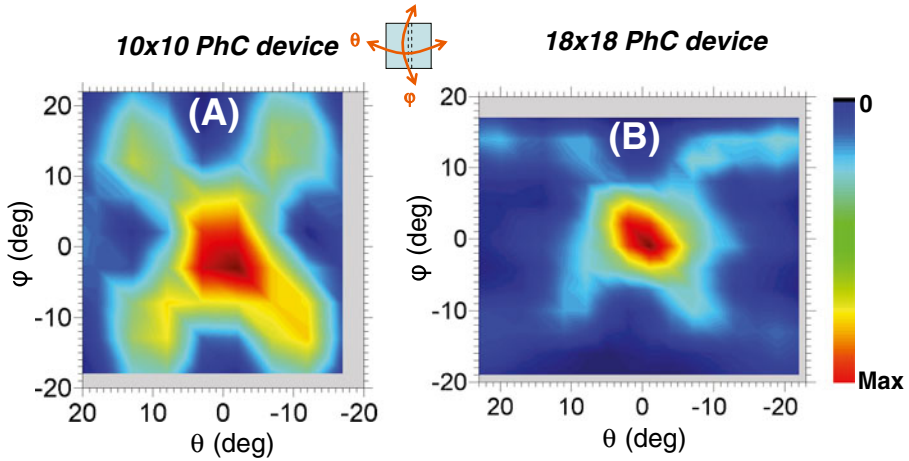
Fig. 5 Typical far-field emission pattern of (A) a 10-by-10 period device and (B) an 18-by-18 period device. The devices are operated in pulsed regime at 25% duty-cycle. The far-field is acquired with a Golay cell detector. The emission is from the surface. The central inset defines the scanning angles

character stems from the introduction of a π phase-shift in the structure, while the beam divergence ($\approx 10 \times 10$ degrees) is related to the total device size. The 10-by-10 period devices still exhibit a strong central, low-divergence beam, but 4 side lateral lobes are clearly visible, an effect related to the smaller device size. Note however that the beam could be simply *cleaned* with a polarizer, since the polarization of the central lobe is orthogonal to the one of the 4 side-lobes.

In order to obtain higher wall-plug efficiencies, we have recently developed surface-emitting THz QC lasers featuring graded photonic heterostructure (GPH) resonators [19]. Figure 6a shows, for a conventional second-order DFB structure with a periodic grating, the transverse magnetic fields (Hy) of the symmetric/radiative and anti-symmetric/non-radiative band-edge modes (at $k_x = 0$). They are located above and below the photonic band gap, respectively. In order to excite the radiative mode - which generally exhibits much higher radiation loss and WPE - we have developed a GPH resonator which consists of a non-
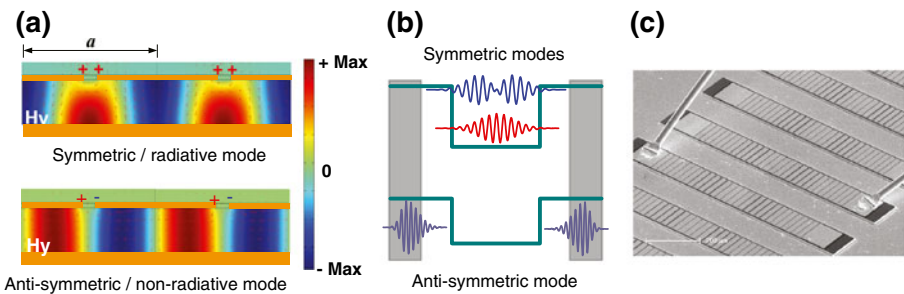
Fig. 6 (a) Transverse magnetic fields (Hy) of the radiative and non-radiative band-edge modes (at $k_x = 0$), located above and below the band gap, respectively [19]. (b) Schematics of the effect induced by the GPH resonator: the radiative modes are confined in the center, while the non-radiative modes are pushed to the highly absorbing device edges, hence they cannot lase. The gray parts highlight the regions where the highly doped n^+ GaAs layers (not covered by metal) induce high losses. (c) Scanning electronic microscope (SEM) images of a typical GPH device

periodic, one-dimensional second-order DFB grating formed on top of the active region [19]. The grating period gradually decreases from the center towards the periphery of the device (Fig. 6c). Such grading introduces a spatially dependent photonic gap with positive curvature, which mimics a type-II potential for photons (Fig. 6b). By analogy with the spatial separation of electron/hole wavefunctions in type-II semiconductor quantum wells, the GPH resonator confines the symmetric/radiative modes in the center of the grating, while it delocalizes the anti-symmetric/non-radiative modes towards the highly lossy device edges (Fig. 6b). The net effect is to force laser operation on a radiative mode, with significantly increased radiation loss and WPE, plus a naturally single-lobed beam pattern [19].

We have implemented GPH resonators with the same QC structure (wafer V414). Figure 7a shows the L-I-V curves at different heat-sink temperatures: the GPH lasers operate up to 85K, with a maximum peak output power of 3.8 mW and a wall-plug efficiency of 0.3% at 12K, which is about 4 times higher than what we obtained in two-dimensional photonic crystal (18×18 periods) lasers. In essence, the GPH lasers provide similar output power to PhC devices, but they are much smaller. This is beneficial for CW operation: since the injection current is not very high, the behavior in CW of these GPH devices is not very different from pulsed operation in terms of power and/or current threshold. Figure 7b highlights that the GPH lasers have a single-lobed far-field emission pattern. The full width at half maximum is 10×32 degrees in the angular directions along and perpendicular to the laser ridge, respectively. The far-field pattern is not as good as the one obtained with PhC lasers, although it is still compatible with most applications. This is a direct consequence of the reduced device size and a necessary compromise to achieve a higher WPE. A more directional beam pattern, especially in the direction perpendicular to the ridge, can be achieved by developing phase-locked arrays of GPH lasers, which would also have higher CW output power.

In conclusion, we have demonstrated two-dimensional arrays of surface-emitting photonic-crystal THz QC lasers. Two different device sizes were explored. The lasers can operate in pulsed or CW regime, up to a maximum operating temperature of 85K in pulsed regime. Typical output powers are sub-mW for the 10-by-10 period devices and of the order of 3 mW for the 18-by-18 period ones. By successively switching the devices of the array on, the array emission frequencies achieve a coverage of ≈170-210 GHz around a central
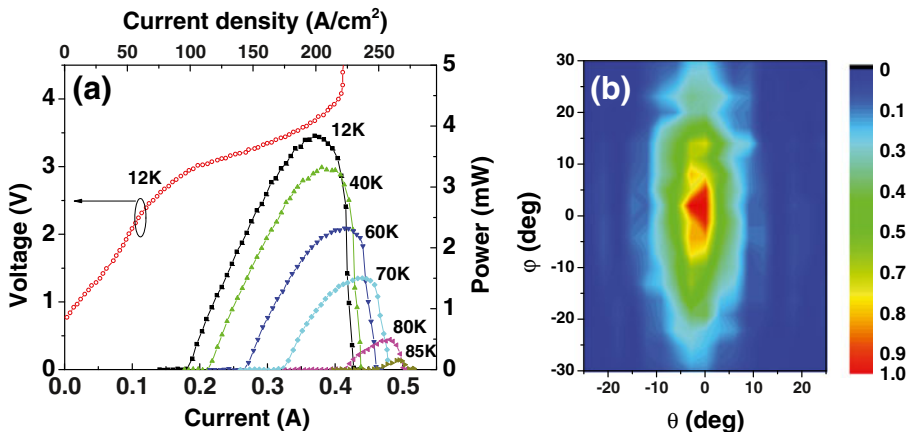
Fig. 7 (a) Light-current–voltage (L-I-V) curves of a typical GPH laser at different heat-sink temperatures, measured in almost-CW regime. The ridge width is 127 μm, the ridge length is 1.46mm, and the single-mode emission frequency is about 2.7 THz. (b) Far-field pattern of the same device measured at 78K

emission frequency of 2.75 THz. The beam pattern quality of the 18-by-18 period devices is excellent (low divergence, single lobed). We have also provided a comparison with surface-emitting lasers based on the concept of graded photonic heterostructure, which significantly improve the wall-plug efficiency .

References

 1. R. Köhler, A. Tredicucci, F. Beltram, H. Beere, E. H. Linfield, A. G. Davies, D. A. Ritchie, R. C. Iotti, F. Rossi, *Nature* **417**, 156–159 (2002).
 2. S. Kumar, C. W. I. Chan, Q. Hu, J. L. Reno, *Nature Phys.* 7, 166, (2010).
 3. S. Fathololoumi, E. Dupont, C. W. I. Chan, Z. R. Wasilewski, S. R. Laframboise, D. Ban, A. Matyas, C. Jirauschek, Q. Hu, H. C. Liu, Optics Express. **20**, 3866 (2012).
 4. Y. Chassagneux, R. Colombelli, W. Maineult, S. Barbieri, H. Beere, D. Ritchie, S. P. Khanna, E. H. Linfield, A. G. Davies, *Nature* **457**, 174–178 (2009).
 5. Y. Chassagneux, R. Colombelli, W. Maineult, S. Barbieri, S. P. Khanna, E. H. Linfield, A. G. Davies, *Appl. Phys. Lett.* **96**, 031104 (2010).
 6. M. I. Amanti, G. Scalari, F. Castellano, M. Beck, J. Faist, *Opt. Express* **18**, 6390–6395 (2010)
 7. T.-Y. Kao, Q. Hu, J. L. Reno, *Opt. Lett.* 37, 2070, (2012).
 8. M. Ravaro, C. Manquest, C. Sirtori, S. Barbieri, G. Santarelli, K. Blary, J.F. Lampin, S.P. Khanna, E.H. Linfield, Opt. Lett. **36**, 3969 (2011).
 9. C. Walther, G. Scalari, M. Amanti, M. Beck, and J. Faist, Science 327, 1495 (2010).
10. E. Strupiechonski, G. Xu, M. Brekenfeld, Y. Todorov, N. Isac, A. M. Andrews, P. Klang, C. Sirtori, G. Strasser, A. Degiron, and R. Colombelli,Appl. Phys. Lett. **100**, 131113 (2012).
11. E. Strupiechonski, G. Xu, P. Cavalié, N. Isac, S. Dhillon, J. Tignon, G. Beaudoin, I. Sagnes, A. Degiron, R. Colombelli, Rapid Comm. Phys. Rev. B **87**, 041408(R) (2013).
12. G. Sevin, D. Fowler, G. Xu, F. H. Julien, R. Colombelli, S. P. Khanna, E. H. Linfield, A.G. Davies, *Appl. Phys. Lett.* **97**, 131101 (2010).
13. L. Sirigu, R. Terazzi, M. I. Amanti, M. Giovannini, J. Faist, L. A. Dunbar, R. Houdré, *Opt. Express* **16**, 5206 (2008).
14. A. Benz, Ch. Deutsch, G. Fasching, K. Unterrainer, A. M. Andrews, P. Klang, W. Schrenk, G. Strasser, *Opt. Express* **17**, 941 (2009)
15. Qi Qin, John L. Reno, and Qing Hu, Opt. Lett. **36**, 692 (2011).
16. L. Mahler, A. Tredicucci, F. Beltram, H. E. Beere, D. A. Ritchie, *Opt. Express* **18**, 19185 (2010)
17. E. Mujagić, C. Schwarzer, Y. Yao, J. Chen, C. Gmachl, G. Strasser, Appl. Phys. Lett. **98**, 141101 (2011).
18. B.G. Lee et al., Appl. Phys. Lett. **91**, 231101 (2007).
19. G. Xu, R. Colombelli, S. P. Khanna, A. Belarouci, X. Letartre, L. Li, E. H. Linfield, A. G. Davies, H. E. Beere, D. A. Ritchie, *Nature Communi.* **3**, 952 (2012)
20. Chassagneux, Y., Palomo, J., Colombelli, R., Barbieri, S., Dhillon, S., Sirtori, C., Beere, H., Alton, J., Ritchie, D., Electron. Lett. **43** (2007).
21. L. Mahler, A. Tredicucci, F. Beltram, C. Walther, J. Faist, H. E. Beere, D. A. Ritchie, Appl. Phys. Lett. **96**, 191109 (2010).